Anharmonic effect driven topological phase transition in PbO₂ predicted by first-principles calculations

Tong Chen, Dexi Shao, Pengchao Lu, Xiaomeng Wang, Juefei Wu, Jian Sun,[*] and Dingyu Xing

National Laboratory of Solid State Microstructures, School of Physics and Collaborative Innovation Center of Advanced Microstructures, Nanjing University, Nanjing 210093, People's Republic of China

The crystal structures and electronic structures of lead dioxide are investigated with *ab initio* calculations. We find the previously known tetragonal β-PbO₂ (space group: $P4_2/mnm$) is dynamically unstable at low temperature due to the existence of a vibrational soft mode under the harmonic approximation, and it becomes stable at finite temperature about 200 K attributed to the enhanced anharmonic effect. Under the guidance of the vibrational soft mode, we find an orthorhombic structure (space group: $Pnnm$) that is a candidate of the ground state of PbO₂ at low temperature. Electronic structure calculations suggest the low-temperature orthorhombic phase is a trivial insulator, while the tetragonal high-temperature phase is a topological Dirac nodal line semimetal. Therefore, there is a topological phase transition from a trivial insulator to a topological semimetal in PbO₂, strongly coupled with the stabilized soft mode and thus anharmonicity-driven structural transformation. For future experiment verification, the results for the temperature dependence of x-ray diffraction and Raman spectra are also provided. Our work demonstrates the important role of anharmonicity in describing the structural phase transition and exploits the impact of anharmonicity to the topological property of the system.

I. INTRODUCTION

Topological materials have been widely studied since they were found to possess novel properties and promising prospects for applications. Topological insulators are materials that are fully gapped in bulk states while having topologically protected gapless edge states [1–4]. These edge states are spin-resolved, and thus they may exhibit great potential in spintronic devices. In addition, a topological insulator has been proposed to be used in quantum computation, as the topological properties of non-Abelian particles are protected by the symmetry of materials, thus a topological insulator can protect quantum coherent states from decoherence and avoid mistakes under perturbations [5]. Topological phase transitions are essential for the emergence of topological phases or their exotic properties. It is significant to find new topological materials and tune parameters for topological transitions. There are various ways to induce a topological transition, e.g., applying pressure [6,7], temperature [8–11], strain [12–14], an external electric field [15], and even introducing disorder [16], etc. From the viewpoint of practicality, one may also be concerned about how temperature can affect the electronic properties of topological materials. Therefore, it is interesting to study temperature-induced topological transitions.

Recently, much attention has been given to researching anharmonicity in elementary substances, compounds, and alloys due to its crucial role in describing the fundamental physical properties of materials. With regard to thermal transport, crystals would show no thermal expansion, and the specific heat would become constant at high temperatures without taking account of the interaction between phonons [17]. With regard to electron-phonon coupling, the anharmonic effect also provides a plausible explanation for the overestimation of the superconducting transition temperature predicted by quasiharmonic theoretical calculations [18]. In addition, anharmonic effects in lattice dynamics are also of crucial importance for temperature-induced structural phase transitions, e.g., in Ti, Zr, Hf [19], Fe [20], and ZrO₂ [21]. However, it has rarely been reported whether the temperature-induced structural phase transition will affect the topological properties in an electronic system.

β-PbO₂ is a material that has been used as the medium in a lead-acid battery for more than 100 years. Unlike other binary metal dioxides such as TiO₂, GeO₂, and SnO₂, which are usually semiconductors [22], β-PbO₂ is reported to be metallic with high-level electrical conductivity [23]. Although β-PbO₂ has been widely used for a long time, it is still unclear whether it is intrinsically a metal or semiconductor; in addition, the origin of its high conductivity is still under debate. Specifically, on the one hand β-PbO₂ was suggested to be intrinsically metallic from experiments, such as x-ray photoelectron spectroscopy, x-ray photoemission spectroscopy, and electron energy-loss spectroscopy [23–27]. Some density functional theory (DFT) calculations based on the conventional generalized gradient approximation with the Perdew-Burke- Ernzerhof functional (GGA-PBE) also suggested that β-PbO₂ is a semimetal with a small overlap between conduction bands and valence bands [25,26,28]. On the other hand, the intrinsic β-PbO₂ was also reported as a semiconductor [29,30], and the high conductivity can arise

*Corresponding address: jiansun@nju.edu.cn

from vacancies [30,31] or the adventitious incorporation of hydrogen [32,33]. Some DFT calculations with more sophisticated Heyd-Scuseria-Ernzerhof (HSE) hybrid functionals showed that β-PbO$_2$ should be a semiconductor with an indirect gap of 0.23 eV [34].

In addition, it is still a mystery whether the lead or oxygen sublattice is substoichiometric [33,35]. Most x-ray photoelectron spectroscopy measurements indicated that the Fermi level was in the conduction bands instead of the energy band gap, which may be attributed to oxygen defects [24]. The loss of oxygen in β-PbO$_2$ was also confirmed by neutron diffraction measurements [34]. However, some neutron diffraction experiments indicated that β-PbO$_2$ was substoichiometric on the cation sublattice while the oxygen sublattice was somehow complete [33,35,36]. In addition, it was reported that PbO$_2$ was a nonstoichiometric oxide of variable composition [37,38]. The loss of oxygen was exothermic and spontaneous in the noninteracting limit, as confirmed by neutron measurements [34]. All of these above-mentioned contradictions show that β-PbO$_2$ is an extremely complicated system and needs to be revisited. In addition, the difficulty of obtaining a pure and stoichiometric phase of β-PbO$_2$ [28,29] also implies to us that it could be thermodynamically or dynamically unstable, and that the real stable phase could still be undiscovered.

In this paper, we study the dynamical property of tetragonal β-PbO$_2$ using *ab initio* calculations. The presence of an imaginary frequency indicates its dynamical instability at low temperature. We identify an orthorhombic phase of PbO$_2$ as the ground state at low temperature by distorting oxygen atoms in β-PbO$_2$ suggested by the soft mode. Theoretical investigation indicates that the tetragonal phase is unstable, but this phase has long been known from experiments. This contradiction may be interpreted as showing that the tetragonal phase is stable only at elevated temperature, where the anharmonic effect plays an important role. We investigate the potential energy surface, anharmonic double-well, and temperature-dependent phonon spectra to prove the strong anharmonic effect in β-PbO$_2$. Electronic structure calculations show that the low-temperature orthorhombic phase is a trivial insulator with a band gap of about 0.12 eV, while the tetragonal phase is a Dirac nodal line (DNL) semimetal. These results suggest that PbO$_2$ may undergo a topological phase transition between a topological trivial insulator and a topological nontrivial semimetal, strongly coupled with a structural phase transition driven by anharmonicity.

II. METHOD

The structural optimization and total energy calculations are performed with the Vienna *ab initio* simulation package (VASP) [39] utilizing the generalized gradient approximation (GGA) in the Perdew-Burke-Ernzerhof (PBE) exchange-correlation functionals [40] and projector augmented-wave (PAW) pseudopotentials [41]. Harmonic phonon spectra are calculated with the PHONOPY package [42]. The temperature-dependent phonon frequencies are evaluated with the self-consistent *ab initio* lattice dynamical (SCAILD) method [19], and the initial displacements are generated by the PHON

program [43] in a $2 \times 2 \times 2$ supercell. Both structures are optimized with kinetic energy for a plane-wave basis cutoff of 700 eV and a Γ-centered $10 \times 10 \times 16$ k-point mesh. The band structures are also checked by nonlocal hybrid functional HSE06 [44] calculations. To investigate the surface states of both phases, tight-binding Hamiltonians are constructed with maximally localized Wannier functions (MLWFs) [45] based on Pb s and p orbitals and O p orbitals, and the semi-infinite surface Green-function method [46] implemented in WANNIERTOOLS [47] is used to construct the surface states. The Raman spectra are calculated with the QUANTUM ESPRESSO package [48] utilizing the local density approximation (LDA) exchange–correlation functionals.

III. RESULTS

A. Dynamical instability with the harmonic approximation and the search for the low-temperature phase

The tetragonal phase β-PbO$_2$ crystallizes with a rutile-type structure (space group: $P4_2/mnm$, No. 136, $Z = 2$) [49]. Each lead atom is connected with six oxygen atoms, while each oxygen atom is connected with three lead atoms. Every six oxygen atoms form an octahedron in which lead is centered. All oxygen atoms are strictly located on either the (110) plane or the ($1\bar{1}0$) plane, as shown in Fig. 1(a).

Although PbO$_2$ has been used in lead acid batteries for more than 100 years, few studies have evaluated its dynamic stability theoretically. We calculate the phonon spectra of β-PbO$_2$ with the harmonic approximation, and we find that an imaginary frequency B_{1g} mode is present at the Γ point. From phonon density of states (PHDOS) analysis, it can be seen that the oxygen atoms contribute the most to the imaginary frequency, as shown in the inset of Fig. 1(e). Figure 1(b) illustrates the vibration of the B_{1g} mode, paralleling with the (001) plane. The lead atoms seem not to participate in the vibration, and the oxygen atoms vibrate around the centered lead atom just like a pendulum, which is in accordance with the PHDOS analysis.

Based on its dynamical instability predicted by our calculations and its thermodynamic instability observed in experiments [28,29], we think that there should be a stable phase at low temperature. After slightly shifting the oxygen atoms according to the vibrational directions of the B_{1g} soft mode and optimizing the atomic positions and cell shape, we obtain an orthorhombic structure (space group: $Pnnm$, No. 58, $Z = 2$). Figure 1(c) shows the top view of an exaggerated structure of the orthorhombic phase. The structural information about the two phases is listed in Table I. Specifically, this orthorhombic structure can be obtained from the tetragonal phase by slightly deviating the oxygen atoms from the (110) plane or the ($1\bar{1}0$) plane in a clockwise direction, stretching along the b axis and compressing along the a axis simultaneously. Therefore, the fourfold screw axis is no longer present, and lattice parameter a is no longer equal to b, which causes the tetragonal structure to degenerate into an orthorhombic structure. The dynamical stability of the orthorhombic phase is confirmed by its phonon dispersions and PHDOS, with no imaginary frequency emergence, as shown in Fig. 1(f).
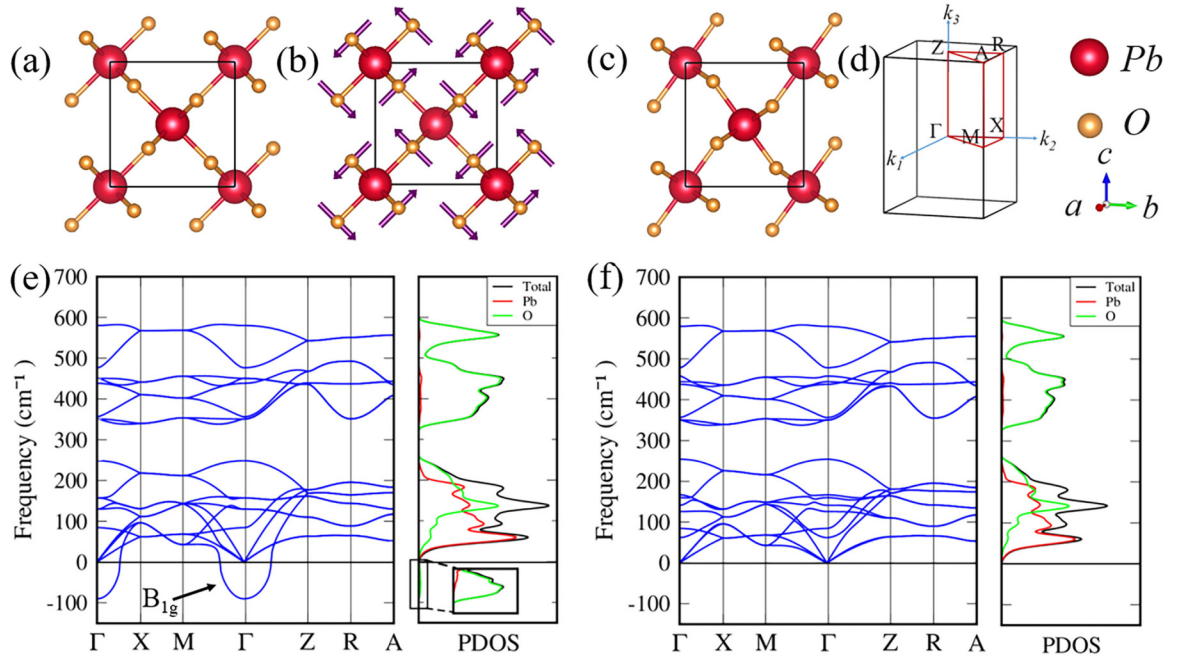
FIG. 1. (a) The top view of the tetragonal phase. The lead and oxygen atoms are distinguished with a red ball and an orange ball. (b) The red arrows piercing though the oxygen atoms point out the imaginary mode vibrational direction calculated with the harmonic approximation. (c) Top view of the exaggerated orthorhombic phase. (d) The Brillouin zone (BZ) and high-symmetry path of the tetragonal phase. (e),(f) The phonon frequencies of the tetragonal (orthorhombic) phase along the high-symmetry lines and the PHDOS obtained by the harmonic approximation.

The $Pnnm$ space group is the maximal subgroup of the $P4_2/mnm$ space group with an index of 2, and the fourfold rotation symmetry is broken during the transition. Meanwhile, the volume is almost the same during the transformation. The phase transition between the $P4_2/mnm$ and $Pnnm$ structure is a continuous second-order phase transition. This phase transition driven by distortions can be viewed as a three-dimensional Peierls-like phase transition. According to Peierls' theory, the energy decrease of the occupied states will exceed the increase of the energy caused by the ionic distortion, and it finally makes the resulting structure more favorable. To confirm the superiority of the $Pnnm$ phase in energy, we calculate the total energy of both phases with several different exchange-correlation functionals, including GGA-PBE, GGA-PW91 [50], and the LDA [51,52]. All the results show that the orthorhombic $Pnnm$ phase is more favorable than tetragonal PbO_2 with $P4_2/mnm$ symmetry. Although the energy difference between the two phases is rather small (about 1 meV), we consider the consistent results from different functionals to be reliable.

B. Anharmonic effect in β-PbO$_2$

The interatomic interactions make some configurations appear at energy saddle points on the potential surface. Thus, the crystal structures of many elements and compounds may not be energetically stable. Sometimes the stability predicted by phonon calculations with the harmonic approximation contradicts with reality, such as the case of β-PbO$_2$. The answer may lie in the fact that the tetragonal phase is stable only if we consider phonon-phonon interaction at finite temperature. Figure 2(a) displays the two-dimensional (2D) potential energy surface of the (001) plane for β-PbO$_2$. The four lead atoms lie in the corner, and the two oxygen atoms lie in the center. It is obvious that the oxygen atom stays in local maxima sites rather than global minima sites. In a continuous second-order phase-transition picture, the free energy has a minimum value in the high-symmetry configuration (β-PbO$_2$) at high temperature, and the same high-symmetry configuration becomes a saddle point if one lowers the temperature. Figure 2(b) shows that the free energy versus displacement curve has a double-well structure at finite displacements of oxygen atoms,

TABLE I. The details of the crystal structures of the tetragonal phase and the orthorhombic phase PbO$_2$.

Phase	Lattice parameter (Å)	Wyckoff position	Atomic coordinates (Fractional)
Tetragonal phase	$a = 5.079$	Pb (2a)	0.5000, 0.5000, 0.5000
($P4_2/mnm$)	$c = 3.446$	O (4g)	0.8079, 0.8079, 0.5000
Orthorhombic phase	$a = 5.054$	Pb (2a)	0.5000, 0.5000, 0.5000
($Pnnm$)	$b = 5.098$	O (4g)	0.2049, 0.8199, 0.5000
	$c = 3.446$		
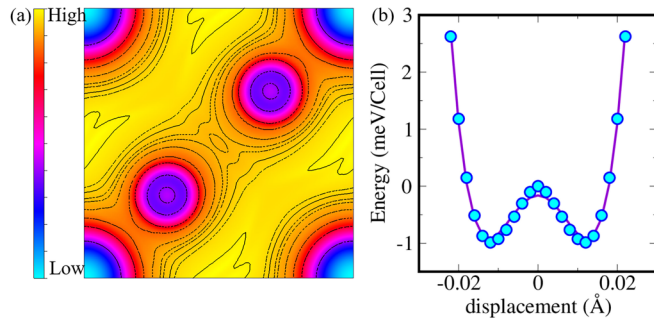
FIG. 2. (a) The 2D potential energy surface of the (001) plane for β-PbO$_2$. (b) The anharmonic double-well potential corresponding to the imaginary B_{1g} mode of β-PbO$_2$. The cyan points are the calculated free energies, and the purple curve is fitted potential energy with a quartic polynomial.

FIG. 3. Temperature-dependent phonon spectra of the tetragonal phase. With the rise of temperature, the imaginary B_{1g} mode gradually vanishes, which makes the tetragonal phase stable at finite temperature.

and it indicates the instability of β-PbO$_2$ below the transition temperature. The reservation of a quartic (fourth) term in the expansion of the potential energy of the displacement of the oxygen atoms from its equilibrium position indicates that the system possesses a strong anharmonic effect, and the fitted curve is known as an anharmonic double-well, which results in the imaginary B_{1g} mode. According to Landau theory of second-order phase transitions, the parameter of the quadratic (second) term should be less than zero so that there are two minima with an order parameter not equal to zero, and the origin of the coordinate will become a saddle point. Meanwhile, the parameter of the quartic (fourth) term of the order parameter should be greater than zero so that the free energy has a minimum for finite values of the order parameter. Our fitted parameter is in agreement with the theory.

With a lattice expansion and compression (from 103% to 97% of the equilibrium volume), the imaginary B_{1g} mode persists all the time, which means that the imaginary mode cannot be eliminated by small tension or pressure. The phonon spectra calculated with the harmonic approximation ignore the anharmonic effect. Therefore, the information that pertains to the temperature dependence of the vibrational modes and the interactions that are responsible for the stability of the high-temperature phase is missing. With the help of SCAILD, which goes beyond the harmonic approximation, it can be proven that the high-temperature tetragonal phase is dynamically stable at elevated temperature, as illustrated in Fig. 3. With rising temperature, the anharmonic interactions become strong, the vibration of the imaginary mode becomes weaker and weaker, and finally the phonon-phonon interactions become strong enough to stabilize the system. The phonon frequencies become real over the whole BZ at 200 K. We thus identify the orthorhombic phase to be the low-temperature phase and the tetragonal phase to be the high-temperature phase, respectively, and the transition temperature is predicted to be about 200 K.

C. Topology of electronic structures affected by anharmonicity

We calculate the electronic structures of these two phases, as shown in Fig. 4. Figure 4(a) depicts the high-temperature
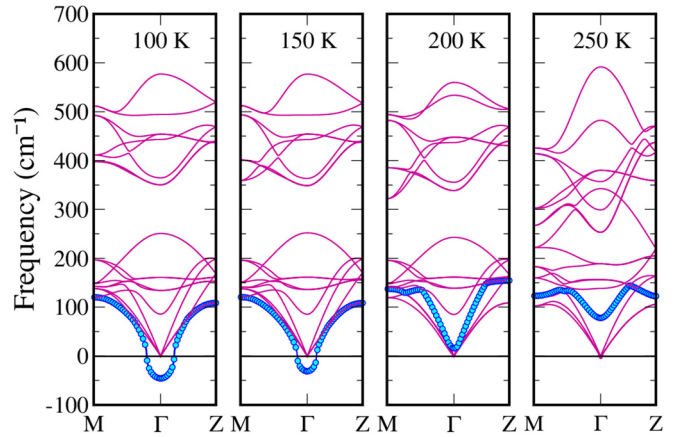
phase with a semimetallic characteristic in the absence of SOC. The highest valence band overlaps the lowest conduction band, forming band reversion at the Γ point, as also mentioned in previous work [53,54]. In view of the big difference between the band structures of the high-temperature phase with different exchange-correlation functionals, i.e., PBE or HSE, as mentioned in previous work [34], we also perform the HSE calculation combined with MLWFs interpolation to describe the band structures accurately. The results show that the overlap between the valence band and the conduction band in the high-temperature phase remains.

As shown in the band-structure calculation of the high-temperature phase in Fig. 4(a), there is a clear signature of band crossing near the Γ point. The little groups along the Γ-M (Γ-Z) lines are C_{2v}(C_{4v}), and the two crossing bands along Γ-M (Γ-Z) belong to different irreducible representations, which means that the band crossings are protected by crystallographic symmetry, shown in Fig. 4(a). As the DNL lies in the mirror plane $(1\bar{1}0)$, the mirror eigenvalue for the two bands is well-defined. The two bands have opposite mirror eigenvalues at one side of the DNL and they swap the mirror eigenvalue when they pass through the nodal line. As for $\sigma_{1\bar{1}0}$, $m = 1$, -1, and -1 for Γ_1, Γ_3, and Γ_4. Thus, the mirror symmetry guarantees the existence of the topological DNL. To identify the nontrivial band topology of the DNL in PbO$_2$, we further study the topologically invariant Berry phase with the form $\gamma = \oint_C \mathcal{A}(\mathbf{k}) \cdot d\mathbf{k}$ [55], where $\mathcal{A}(\mathbf{k})$ is the Berry connection of the occupied states, and C is a closed loop in momentum space. If C is pierced by the node line, one has $\gamma = \pi$, otherwise $\gamma = 0$. We get $\gamma = \pi$, which indicates that this nodal line is protected by the nontrivial Berry phase.

To provide more insights into the DNLs surrounding the Γ point, we establish an effective Hamiltonian model using the $\mathbf{k} \cdot \mathbf{p}$ method. We find that band inversion between O p and Pb s orbits contributes to the formation of the DNLs around the Γ point. Taking the crystal symmetry and the time-reversal symmetry (TRS) into consideration, the effective Hamiltonian
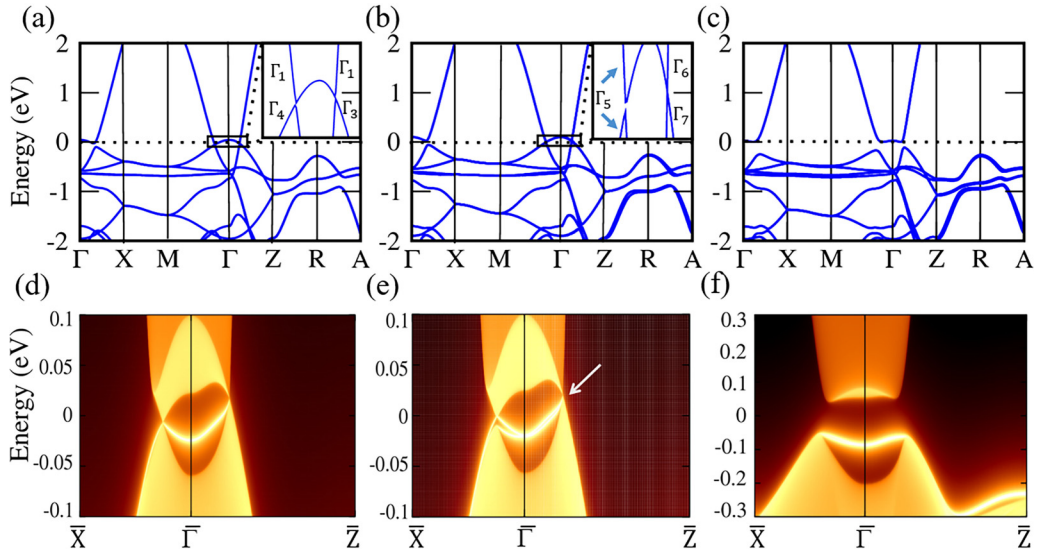
FIG. 4. Band structures of (a) the high-temperature phase without SOC, (b) the high temperature phase with SOC, and (c) the low-temperature phase with SOC. The semi-infinite surface states in (d) the (100) surface of the high-temperature phase without SOC, (e) the high-temperature phase with SOC, and (f) the low-temperature phase with SOC. The arrow in (e) marks the projection of the Dirac point.

can be written as

$$H(\mathbf{k}) = g_0(\mathbf{k})\tau_0 + g_x(\mathbf{k})\tau_x + g_z(\mathbf{k})\tau_z,$$

$$g_0(\mathbf{k}) = M_0 - B_0(k_x^2 + k_y^2) - C_0 k_z^2,$$

$$g_x(\mathbf{k}) = A(k_x^2 - k_y^2),$$

$$g_z(\mathbf{k}) = M_z - B_z(k_x^2 + k_y^2) - C_z k_z^2.$$

Here, τ_x and τ_z are Pauli matrices, and τ_0 is a 2×2 unit matrix. This system has both TRS and inversion symmetry (IS), thus the component of τ_y must be zero [56]. We can obtain the eigenvalues of this two-level system by diagonalizing the 2×2 effective Hamiltonian, and the results give $E(\mathbf{k}) = g_0(\mathbf{k}) \pm \sqrt{g_x^2(\mathbf{k}) + g_z^2(\mathbf{k})}$. Band crossing of the DNL occurs when $g_x(\mathbf{k}) = g_z(\mathbf{k}) = 0$. In fact, $M_z B_z > 0 \cap M_z C_z > 0$, which gives $g_z(\mathbf{k}) = 0$, is exactly the condition of band inversion between $|\text{Pb}s\rangle$ and $|\text{O}p\rangle$ orbitals. Furthermore, $g_z(\mathbf{k}) = 0$ gives a nodal ellipsoid in the BZ around the Γ point, while $g_x(\mathbf{k}) = 0$ confines the band crossing of the DNLs in the $k_x = \pm k_y$ planes. Therefore, there are two DNLs located on the two Γ-M-Z planes perpendicular to each other.

SOC, which breaks the SU(2) symmetry, will induce a pair of Dirac points related to each other by TRS along the Γ-Z direction while inducing a small gap about 10 meV elsewhere. As shown in Fig. 4(b), along the Γ-M direction the valence-band maxima (VBM) and conduction-band minimum (CBM) have the same irreducible representation Γ_5, which allows the hybridization between them, while in the Γ-Z direction the two relevant bands belong to two different irreducible representations (Γ_6 and Γ_7), and the hybridization between these two bands is forbidden.

SOC couples the spin and orbital angular momentum, which generates a group of eigenstates with certain total angular momentum quantum numbers. We can denote these eigenstates of the CBM and VBM as $|\text{Pb}_s^+, \mp\frac{1}{2}\rangle$ and $|\text{O}_p^+, \mp\frac{1}{2}\rangle$, respectably. Here, the subscripts s and p denote corresponding

orbit components of the eigenstates, and the superscripts "$\mp$" represent the parities of the corresponding eigenstates. Taking the D_{4h} point group and TRS into consideration, our model Hamiltonian becomes

$$H(\mathbf{k}) = \epsilon_0(\mathbf{k}) + \sum_{i=1}^{5} f_i(\mathbf{k}) \cdot \Gamma_i$$

$$= \epsilon_0(\mathbf{k}) + \begin{pmatrix} M(\mathbf{k}) & 0 & A(\mathbf{k}) & C(\mathbf{k}) \\ 0 & M(\mathbf{k}) & C^*(\mathbf{k}) & -A^*(\mathbf{k}) \\ A^*(\mathbf{k}) & C(\mathbf{k}) & -M(\mathbf{k}) & 0 \\ C^*(\mathbf{k}) & -A(\mathbf{k}) & 0 & -M(\mathbf{k}) \end{pmatrix},$$

which describes the dispersion of the VBM and CBM around the Γ point. Here we use the following Γ matrices:

$$\Gamma_1 = \sigma_3 \otimes \tau_0 \quad \Gamma_2 = \sigma_1 \otimes \tau_3 \quad \Gamma_1 = \sigma_2 \otimes \tau_0,$$
$$\Gamma_4 = \sigma_1 \otimes \tau_1 \quad \Gamma_5 = \sigma_1 \otimes \tau_2,$$

which satisfies the Clifford algebra $\{\Gamma_a, \Gamma_b\} = 2\delta_{ab}$, while the other 10 Γ matrices are given by $\Gamma_{ab} = \frac{1}{2i}[\Gamma_a, \Gamma_b]$. The presence of both TRS and IS will prevent the existence of these 10 Γ_{ab} terms in our model Hamiltonian. It can then be written as

$$\epsilon_0(\mathbf{k}) = D_0 - m_0 k_z^2 - n_0(k_x^2 + k_y^2),$$
$$M(\mathbf{k}) = D_1 - m_1 k_z^2 - n_1(k_x^2 + k_y^2),$$
$$A(\mathbf{k}) = D_2 k_x k_y(k_x^2 - k_y^2) - i(D_3 - m_3 k_z^2),$$
$$C(\mathbf{k}) = D_4 k_y k_z - i D_4 k_x k_z.$$

From the model Hamiltonian together with the band structures shown in Fig. 4(b), we can draw the following conclusions. First, $\epsilon_0(\mathbf{k})$ will break the particle-hole symmetry for the CBM and VBM around the Γ point. Second, D_1 in $M(\mathbf{k})$ will open a gap at the Γ point. Third, to reproduce band inversion, we must have $D_1 m_1 > 0 \cap D_1 n_1 > 0$. The
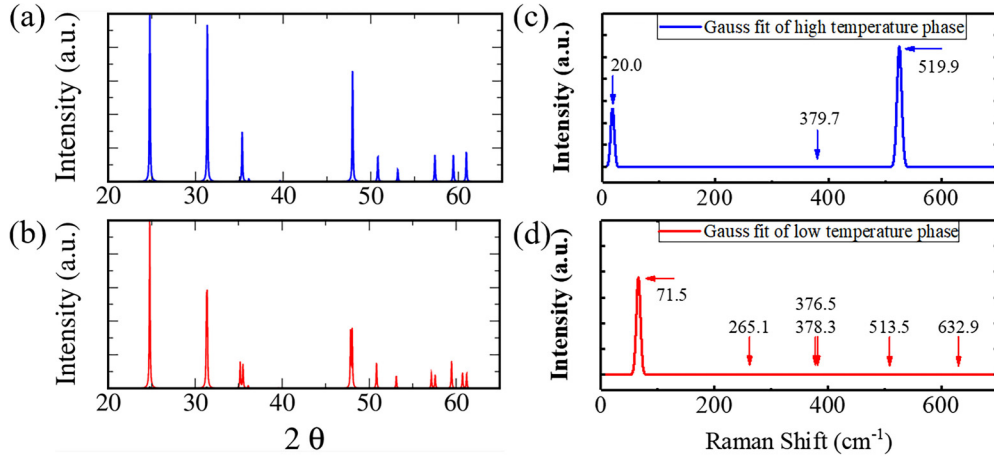
FIG. 5. The calculated XRD patterns of the high-temperature phase (a) and the low-temperature phase (b). Parts (c) and (d) are calculated Raman spectra with Gaussian fitting of the high-temperature phase and the low-temperature phase. The arrows in (c) and (d) and the numbers above them show the peak positions of the calculated Raman modes, where some low-intensity Raman modes are presented.

dispersions of the model Hamiltonian can be given as

$$E(\boldsymbol{k}) = f_0(\boldsymbol{k})$$
$$\pm \sqrt{f_1^2(\boldsymbol{k}) + f_2^2(\boldsymbol{k}) + f_3^2(\boldsymbol{k}) + f_4^2(\boldsymbol{k}) + f_5^2(\boldsymbol{k})} \,,$$

and both dispersions are doubly degenerate. As a result, the band crossing of this model requires

$$f_1 = f_2 = f_3 = f_4 = f_5 = 0,$$

i.e., $k_x = k_y = 0 \cap D_3 m_3 = \frac{D_1}{m_1} < 0$. Along the $k_x = k_y = 0$ line, we have $f_{2,4,5} = 0$. On the one hand, the effect of SOC is small, which leads to $f_3 \to 0$; on the other hand, $D_1 m_1 > 0$ is simply the condition of band inversion between the CBM and the VBM. Thus, the Dirac points protected by R_{4z} symmetry appear at $k = (0, 0, k_c)$, $k_c = \pm\sqrt{\frac{D_1}{m_1}}$.

As for the topological DNL, one of the most important signatures is the two-dimensional drumhead-like surface states. The semi-infinite surface state along the [100] direction is shown in Fig. 4(d). The nontrivial surface states connecting the touching points in the enclosed region exist near the Fermi level around the Γ point. The drumhead-like surface state connecting the two projected Dirac points is highlighted with the brightest line. When considering SOC, the topological DNL evolves into a pair of Dirac points in the Γ-Z direction, as shown in Fig. 4(e). The nontrivial surface states emerge from the projected Dirac point marked with a gray arrow.

Figures 4(c) and 4(f) depict the band structures and surface states of the low-temperature phase with the characteristic of an insulator. The B_{1g} mode, which can only be stabilized by a strong anharmonic effect, makes the high-temperature phase unstable when the strength of the anharmonicity becomes weak at low temperature. It moves all the oxygen atoms off the (110) and (1$\bar{1}$0) planes, and thus it destroys the mirror planes in which the DNLs are located, and it breaks the equivalence of the a-axis and the b-axis of the crystal. Because of the loss of the protection of mirror symmetry and the band gap induced by the distortion of the oxygen atoms, the DNLs no longer exist. In the low-temperature phase, the lowest conduction band and the highest valence band are separated

by an energy gap of about 0.12 eV. The calculated Z_2 index for the low-temperature phase using the Wilson loop method [57,58] is $(v0; v1, v2, v3) = (0; 0, 0, 0)$, which indicates that the low-temperature phase is a trivial insulator. Figure 4(f) displays its trivial surface state on the (100) surface without any nontrivial topological surface states lying in the band gap.

For future experimental verification, Fig. 5 illustrates a comparison of x-ray diffraction (XRD) patterns and Raman spectra between the two phases. The green and red curves represent high-temperature and low-temperature phase Raman spectra, respectively. For XRD patterns, the positions of most of the peaks are the same between the two phases. However, there are several single peaks splitting into a doublet at 35.92°, 47.96°, 57.36°, and 60.96° for the low-temperature phase. The distinction for the Raman spectra of the two phases is obvious, as can be seen in Figs. 5(c) and 5(d). Figures 5(c) and 5(d) label the major peaks with Gaussian fitting for the two phases. In addition, there are also some peaks with a relatively weak signal that may be detected: 379.7 and 636.3 cm^{-1} for the high-temperature phase and 265.1, 376.5, 378.3, 513.5, and 632.9 cm^{-1} for the low-temperature phase.

IV. CONCLUSIONS

In summary, by using *ab initio* calculations we investigate the dynamical behavior of tetragonal PbO$_2$ and find it is unstable under the harmonic approximation. Guided by its soft mode, we distort the oxygen atoms and obtain a dynamical stable orthorhombic phase *Pnnm* after full optimization. In view of the limitations of the harmonic approximation in dealing with a system with a strong anharmonic effect, we investigate the surface potential of the tetragonal phase and discover that the oxygen atoms are lying in the saddle points rather than global minima sites, which is also confirmed by the anharmonic double well. To verify the strong anharmonicity in the tetragonal phase, we study its dynamical behavior at finite temperature and prove that the tetragonal phase can be stabilized at elevated temperature. We conclude that the orthogonal phase is a low-temperature phase and the already known tetragonal phase is a high-temperature phase with a

transition temperature of about 200 K. Combined with the phase transition caused by anharmonicity with increasing temperature, the electronic structures change from semiconductor to semimetal, and the topological property changes from trivial to nontrivial. Finally, we provide theoretical XRD and Raman spectra results for these two phases for future experimental verification.

[1] H. Zhang, C.-X. Liu, X.-L. Qi, X. Dai, Z. Fang, and S.-C. Zhang, Nat. Phys. **5**, 438 (2009).

[2] Y. Xia, D. Qian, D. Hsieh, L. Wray, A. Pal, H. Lin, A. Bansil, D. Grauer, Y. S. Hor, R. J. Cava *et al.*, Nat. Phys. **5**, 398 (2009).

[3] X.-L. Qi and S.-C. Zhang, Rev. Mod. Phys. **83**, 1057 (2011).

[4] M. Z. Hasan and J. E. Moore, Annu. Rev. Condens. Matter Phys. **2**, 55 (2011).

[5] C. Nayak, S. H. Simon, A. Stern, M. Freedman, and S. Das Sarma, Rev. Mod. Phys. **80**, 1083 (2008).

[6] Y. Zhou, P. Lu, Y. Du, X. Zhu, G. Zhang, R. Zhang, D. Shao, X. Chen, X. Wang, M. Tian *et al.*, Phys. Rev. Lett. **117**, 146402 (2016).

[7] Z. Guo, P. Lu, T. Chen, J. Wu, J. Sun, and D. Xing, Sci. China Phys. Mech. Astron. **61**, 038211 (2018).

[8] P. Dziawa, B. J. Kowalski, K. Dybko, R. Buczko, A. Szczerbakow, M. Szot, E. Łusakowska, T. Balasubramanian, B. M. Wojek, M. H. Berntsen *et al.*, Nat. Mater. **11**, 1023 (2012).

[9] B. M. Wojek, M. H. Berntsen, V. Jonsson, A. Szczerbakow, P. Dziawa, B. J. Kowalski, T. Story, and O. Tjernberg, Nat. Commun. **6**, 8463 (2015).

[10] G. Antonius and S. G. Louie, Phys. Rev. Lett. **117**, 246401 (2016).

[11] Y. Zhang, C. Wang, L. Yu, G. Liu, A. Liang, J. Huang, S. Nie, X. Sun, Y. Zhang, B. Shen *et al.*, Nat. Commun. **8**, 15512 (2017).

[12] J. Ruan, S.-K. Jian, H. Yao, H. Zhang, S.-C. Zhang, and D. Xing, Nat. Commun. **7**, 11136 (2016).

[13] D. Shao, J. Ruan, J. Wu, T. Chen, Z. Guo, H. Zhang, J. Sun, L. Sheng, and D. Xing, Phys. Rev. B **96**, 075112 (2017).

[14] D. Shao, T. Chen, Q. Gu, Z. Guo, P. Lu, J. Sun, L. Sheng, and D. Xing, Sci. Rep. **8**, 1467 (2018).

[15] J. Li and K. Chang, Appl. Phys. Lett. **95**, 222110 (2009).

[16] M. Brahlek, N. Koirala, M. Salehi, J. Moon, W. Zhang, H. Li, X. Zhou, M.-G. Han, L. Wu, T. Emge *et al.*, Phys. Rev. B **94**, 165104 (2016).

[17] R. A. Cowley, Adv. Phys. **12**, 421 (1963).

[18] I. Errea, M. Calandra, C. J. Pickard, J. Nelson, R. J. Needs, Y. Li, H. Liu, Y. Zhang, Y. Ma, and F. Mauri, Phys. Rev. Lett. **114**, 157004 (2015).

[19] P. Souvatzis, O. Eriksson, M. I. Katsnelson, and S. P. Rudin, Phys. Rev. Lett. **100**, 095901 (2008).

[20] W. Luo, B. Johansson, O. Eriksson, S. Arapan, P. Souvatzis, M. I. Katsnelson, and R. Ahuja, Proc. Natl. Acad. Sci. (USA) **107**, 9962 (2010).

[21] P. Souvatzis and S. P. Rudin, Phys. Rev. B **78**, 184304 (2008).

[22] R. D. Shannon and R. X. Fischer, Phys. Rev. B **73**, 235111 (2006).

[23] D. A. J. Rand, J. Power Sources **4**, 252 (1979).

[24] D. J. Payne, R. G. Egdell, W. Hao, J. S. Foord, A. Walsh, and G. W. Watson, Chem. Phys. Lett. **411**, 181 (2005).

[25] D. J. Payne, R. G. Egdell, D. S. L. Law, P.-A. Glans, T. Learmonth, K. E. Smith, J. Guo, A. Walsh, and G. W. Watson, J. Mater. Chem. **17**, 267 (2007).

[26] D. J. Payne, R. G. Egdell, G. Paolicelli, F. Offi, G. Panaccione, P. Lacovig, G. Monaco, G. Vanko, A. Walsh, G. W. Watson *et al.*, Phys. Rev. B **75**, 153102 (2007).

[27] D. J. Payne, G. Paolicelli, F. Offi, G. Panaccione, P. Lacovig, G. Beamson, A. Fondacaro, G. Monaco, G. Vanko, and R. G. Egdell, J. Electron. Spectrosc. Relat. Phenom. **169**, 26 (2009).

[28] M. Heinemann, H. J. Terpstra, C. Haas, and R. A. de Groot, Phys. Rev. B **52**, 11740 (1995).

[29] W. Mindt, J. Electrochem. Soc. **116**, 1076 (1969).

[30] S. R. Ellis, N. A. Hampson, M. C. Ball, and F. Wilkinson, J. Appl. Electrochem. **16**, 159 (1986).

[31] X. Li, D. Pletcher, and F. C. Walsh, Chem. Soc. Rev. **40**, 3879 (2011).

[32] P. T. Moseley, J. L. Hutchison, C. J. Wright, M. A. M. Bourke, R. I. Hill, and V. S. Rainey, J. Electrochem. Soc. **130**, 829 (1983).

[33] P. Ruetsch, J. Electrochem. Soc. **139**, 1347 (1992).

[34] D. O. Scanlon, A. B. Kehoe, G. W. Watson, M. O. Jones, W. I. F. David, D. J. Payne, R. G. Egdell, P. P. Edwards, and A. Walsh, Phys. Rev. Lett. **107**, 246402 (2011).

[35] J. D. Jorgensen, R. Varma, F. J. Rotella, G. Cook, and N. P. Yao, J. Electrochem. Soc. **129**, 1678 (1982).

[36] R. J. Hill, Mater. Res. Bull. **17**, 769 (1982).

[37] G. Butler and J. L. Copp, J. Chem. Soc. **145**, 725 (1956).

[38] W. Fischer and H. Rickert, Ber. Bunsenges. Phys. Chem. **77**, 975 (1973).

[39] G. Kresse and J. Furthmüller, Phys. Rev. B **54**, 11169 (1996).

[40] J. P. Perdew, K. Burke, and M. Ernzerhof, Phys. Rev. Lett. **78**, 1396 (1997).

[41] G. Kresse and D. Joubert, Phys. Rev. B **59**, 1758 (1999).

[42] A. Togo and I. Tanaka, Scr. Mater. **108**, 1 (2015).

[43] D. Alfè, Comput. Phys. Commun. **118**, 31 (1999).

[44] A. V. Krukau, O. A. Vydrov, A. F. Izmaylov, and G. E. Scuseria, J. Chem. Phys. **125**, 224106 (2006).

[45] A. A. Mostofi, J. R. Yates, Y.-S. Lee, I. Souza, D. Vanderbilt, and N. Marzari, Comput. Phys. Commun. **178**, 685 (2008).

[46] M. P. L. Sancho, J. M. L. Sancho, J. M. L. Sancho, and J. Rubio, J. Phys. F **15**, 851 (1985).

[47] S. Z. Quan Sheng Wu, H.-F. Song, M. Troyer, and A. A. Soluyanov, Comput. Phys. Commun. **224**, 405 (2018).

[48] G. Paolo, B. Stefano, B. Nicola, C. Matteo, C. Roberto, C. Carlo, C. Davide, L. C. Guido, C. Matteo, D. Ismaila *et al.*, J. Phys. Condens. Matter **21**, 395502 (2009).

[49] H. Harada, Y. Sasa, and M. Uda, J. Appl. Cryst. **14**, 141 (1981).

[50] J. P. Perdew, K. Burke, and Y. Wang, Phys. Rev. B **54**, 16533 (1996).

[51] W. Kohn and L. J. Sham, Phys. Rev. **137**, A1697 (1965).

[52] J. P. Perdew and Y. Wang, Phys. Rev. B **45**, 13244 (1992).

[53] Z. Wang and G. Wang, Phys. Lett. A **381**, 2856 (2017).

[54] W. Wang, L. Deng, N. Jiao, P. Zhou, and L. Sun, Phys. Status Solidi RRL **11**, 1700271 (2017).

[55] S. Ryu and Y. Hatsugai, Phys. Rev. Lett. **89**, 077002 (2002).

[56] H. Weng, Y. Liang, Q. Xu, R. Yu, Z. Fang, X. Dai, and Y. Kawazoe, Phys. Rev. B **92**, 045108 (2015).

[57] A. A. Soluyanov and D. Vanderbilt, Phys. Rev. B **83**, 035108 (2011).

[58] R. Yu, X. L. Qi, A. Bernevig, Z. Fang, and X. Dai, Phys. Rev. B **84**, 075119 (2011).